

## Melt distribution in olivine rocks based on electrical conductivity measurements

Saskia M. ten Grotenhuis, Martyn R. Drury, Chris J. Spiers, and Colin J. Peach

Department of Earth Sciences, Utrecht University, Utrecht, Netherlands

Received 1 October 2004; revised 18 March 2005; accepted 14 September 2005; published 9 December 2005.

[1] Properties of partially molten rocks depend strongly on the grain-scale melt distribution. Experimental samples show a variety of microstructures, such as melt lenses, layers, and multigrain melt pools, which are not readily explained using the theory for melt distribution based on isotropic interface energies. These microstructures affect the melt distribution and the porosity-permeability relation. It is still unclear how the melt distribution changes with increasing melt fraction. In this study, electrical conductivity measurements and microstructural investigation with scanning electron microscopy and electron backscatter diffraction are combined to analyze the melt distribution in synthetic, partially molten, iron-free olivine rocks with 0.01–0.1 melt fraction. The electrical conductivity data are compared with the predictions of geometric models for melt distribution. Both the conductivity data and the microstructural data indicate that there is a gradual change in the melt distribution with melt fraction ( $X_m$ ) between 0.01 and 0.1. At a melt fraction of 0.01, the melt is situated in a network of triple junction tubes, and almost all grain boundaries are free from melt layers. At 0.1, the melt is situated in a network of grain boundary melt layers, as well as occupying the triple junctions. Between melt fractions 0.01 and 0.1, the number of grain boundary melt layers increases gradually. The electrical conductivity of the partially molten samples is best described by Archie's law ( $\sigma_{\text{sample}}/\sigma_{\text{melt}} = CX_m^n$ ) with parameters  $C = 1.47$  and  $n = 1.30$ .

**Citation:** ten Grotenhuis, S. M., M. R. Drury, C. J. Spiers, and C. J. Peach (2005), Melt distribution in olivine rocks based on electrical conductivity measurements, *J. Geophys. Res.*, 110, B12201, doi:10.1029/2004JB003462.

### 1. Introduction

[2] The geometry of the three-dimensional melt network in partially molten mantle rocks is important in controlling phenomena such as melt segregation and migration, and plays a key role in determining the geodynamic evolution of mid ocean ridges and island arcs [Turcotte and Morgan, 1992]. Melt distribution is classically considered to be determined by minimization of interfacial energy, in a static environment or at low strain rates where an equilibrium state can be reached [Bulau and Waff, 1979; McKenzie, 1984]. In the framework of this equilibrium thermodynamics approach, perfect triple junction interconnectivity of the melt is predicted in a single mineral system, with uniform isotropic grains, when the equilibrium dihedral wetting angle ( $\theta_{\text{eq}}$ ) at two-grain junctions is smaller than  $60^\circ$  [Kingery et al., 1976; Bulau and Waff, 1979]. This applies regardless of the liquid fraction. The intervening two-grain junctions are predicted to be melt free as long as the equilibrium dihedral angle is larger than zero. However, in natural and experimentally produced partially molten samples with  $\theta_{\text{eq}} \leq 60^\circ$ , the distribution differs considerably from the predicted geometry because of anisotropy of surface energies and disequilibrium features [Laporte and

Provost, 2000]. As pointed out by Waff and Faul [1992], an additional factor playing a role here is that only a small variation in the ratio of solid-solid to solid-liquid interfacial energy is needed to cover the range of dihedral wetting angles from 0 to  $60^\circ$ .

[3] Numerous high-temperature experimental studies on partially molten mantle rocks and dunite with added mafic or ultramafic melt, have been performed to determine the equilibrium dihedral wetting angles and to verify the classical theoretical predictions for melt distribution in geological materials. The microstructures resulting from these experiments were generally quenched and studied with scanning electron microscopy (SEM) and transmission electron microscopy (TEM). Estimates of the equilibrium dihedral wetting angle ( $\theta_{\text{eq}}$ ) in olivine in contact with basaltic melts give values between 20 and  $50^\circ$  [Faul, 2000; Waff and Bulau, 1979]. However, direct high-resolution measurements with TEM indicate significantly smaller dihedral angles, between 0 and  $10^\circ$ , for equilibrium triple junction geometries with curved crystal-melt interfaces [Cmiral et al., 1998]. Besides triple junctions with curved grain-melt interfaces, a number of different melt microstructures have been reported, caused by anisotropy of olivine interfacial energies [Cmiral et al., 1998; de Kloe, 2001], such as melt layers and interspersed bounding straight crystal faces, and melt pockets adjacent to subgrain boundaries. Drury and Fitz Gerald [1996] and de Kloe et al. [2000]

concluded that melt is present in very thin (nanometer-scale) films on all the grain boundaries and in the triple junctions, on the basis of TEM studies of experimental olivine and orthopyroxene samples.

[4] Studies of melt distribution have been used to predict porosity-permeability relations for partially molten mantle rocks with the aim of providing the basic data needed for quantifying melt segregation and migration behavior. *Faul et al.* [1994] and *Faul* [1997, 2001] separate the melt inclusions into two categories. Most of the melt is situated in disc shaped inclusions or melt layers on two-grain boundaries, the remainder in a network of tubes along triple junctions. Only when the melt discs are connected, above 2–3% melt, does the permeability increase significantly. *Wark and Watson* [1998], *Wark et al.* [2003], and *Hiraga et al.* [2002] on the other hand argue that most melt is present in a triple junction network, based on serial sectioning and TEM, respectively. These studies suggest a continuous porosity-permeability function. By contrast, *Hirth and Kohlstedt* [1995] performed deformation experiments in the diffusion creep regime on partially molten dunite. They observed a strain rate enhancement at melt fractions above 0.05, above which a significant fraction of two-grain boundaries became wetted by melt, forming rapid transport paths. *Walte et al.* [2003] studied fluid distribution using an analogue system norcamphor and ethanol see-through experiments. They conclude that static grain growth in partially molten samples gives a range of transient melt features, corresponding to metastable structures in melt distribution, like multigrain melt pools and melt lenses along grain boundaries. Although these are not real rock experiments, they give new insight into the way transient melt features influence the melt distribution.

[5] Previous microstructural and experimental studies of melt distribution are thus inconsistent and inconclusive. In part, this may reflect that there are several problems inherent to microscopy studies of melt distribution. One is that the melt distribution in a sample at the melting temperature might not be exactly the same as the glass distribution in a quenched sample, for example, if the pore configuration re-equilibrates quickly during quenching. Additionally, the melt distribution can only be studied in 2D, or in a small volume by serial sectioning. This yields incomplete data on dihedral wetting angles and melt distribution. Interpretation of high-resolution TEM images is also ambiguous, as similar images can be interpreted in different ways [*de Kloe et al.*, 2000; *Hiraga et al.*, 2002]. The implication is that a real-time, in situ method of studying melt distribution is needed. Since melt films, layers and tubes are generally fast diffusion paths, frequency-dependent measurements of the electrical properties of partially molten samples can give such an indication of the melt distribution, in situ, while the sample is maintained above the melting temperature. This is because the bulk conductivity of partial melts depends, not only on melt conductivity and melt fraction, but also on the melt distribution. Such effects of melt distribution have been determined for the system  $\text{H}_2\text{O}_{\text{ice}}\text{-KCl}_{\text{aqueous}}$  studied by *Watanabe and Kurita* [1993] as an analogue for partially molten rocks, because this system allows accurate control of the amount of melt present. They observed that the

increase in conductivity with increasing melt fraction follows Archie's law, which in their case represents a gradual change from isolated fluid pores at low melt fractions to a triple junction network at high melt fractions.

[6] The number of such conductivity studies on partially molten rocks is very limited. *Sato and Ida* [1984] measured the electrical conductivity of partially molten gabbro, and concluded that connected melt contributes to the increase in bulk conductivity in the range of melt fraction 0–17% and that melt pockets mainly cause ionic polarization. *Roberts and Tyburczy* [1999] investigated the electrical response of a mixture of 95% olivine ( $\text{Fo}_{80}$ ) with 5% MORB. They varied the melt fraction by varying the temperature. Bulk conductivity was modeled by the Hashin-Shtrikman upper bound [*Hashin and Shtrikman*, 1962], and by Archie's law. The disadvantages of their approach are that the melt composition varies drastically with temperature, that melt fraction and conductivity both have to be estimated using thermodynamic calculations, and that the range of melt fraction explored is limited in their study. A systematic, in situ study of the melt distribution at different melt fractions in partially molten rocks is therefore still lacking. Although in the mantle melt fraction and composition are more likely to be affected by temperature rather than isothermal substitutions, a study in which the melt fraction is varied independently of temperature effects is still needed to determine the relationship between melt fraction and melt distribution, and to assess the consequences of this for porosity-permeability relations in partially molten mantle rocks. A remaining question is whether the changes in melt distribution with increasing melt fraction are gradual or discontinuous.

[7] In this study, we will present new conductivity measurements on partially molten olivine rocks. The system we have chosen consists of synthetically produced forsterite-enstatite ( $\text{Mg}_2\text{SiO}_4\text{-MgSiO}_3$ ) ceramic with an added melt/glass composed of 29% MgO, 20%  $\text{Al}_2\text{O}_3$  and 51%  $\text{SiO}_2$ . The amount of glass added to the ceramic is varied between 1 and 10%. The chemical composition of the glass was chosen in such a manner that the equilibrium melt content of the partial melt at the studied temperature is equivalent to the amount of the melt/glass added to the sample. In this way, complex phase relationships can be avoided and the amount of melt in the samples can be controlled accurately simply through the amount added to the sample. The results are compared with predictions made using geometric models incorporating different arrangements of melt and grains. This enables us to determine the melt distribution in the samples while they are partially molten. After the experiments, the samples were also studied with scanning electron microscopy (SEM), and electron backscatter diffraction (EBSD), to verify the conclusions drawn from the conductivity measurements.

## 2. Method

### 2.1. Sample Preparation

[8] In our approach, two methods are used to prepare disc-shaped samples measuring 10 mm diameter and 1–1.5 mm thickness. For samples containing a melt fraction

**Table 1.** Samples<sup>a</sup>

Sample	Added Melt Content, %	Melt Content From EBSD and SEM, %	Sinter Time, min	Final Grain Size, $\mu\text{m}$
Fo9	10.0	9.67	180	25.7
Fo8	5.0	5.23	180	ND
Fo20	3.5	3.42	240	39.5
Fo11	2.5	2.55	240	ND
Fo22	1.5	1.67	240	50.5
Fo23	1.5	1.47	120	48.3
Fo24	1.0	1.39	240	32.3
Fo26	1.0	ND	240	ND
Fo27	3.5	3.27	4800	ND
Fo28	1.5	1.54	4800	ND

<sup>a</sup>ND means not determined for these samples.

of 0.025–0.1, synthetic polycrystalline discs are made, using the sol gel and powder processing method described by *McDonnell et al.* [2002]. These samples consist of 95% forsterite (Fo,  $\text{Mg}_2\text{SiO}_4$ ) and 5% enstatite (En,  $\text{MgSiO}_3$ ), the iron free end-members of olivine and pyroxene, respectively. They have a fine grain size of about 1  $\mu\text{m}$ , and a porosity of 13–14%. The synthetic basaltic melt, consisting of 29% MgO, 51%  $\text{SiO}_2$  and 20%  $\text{Al}_2\text{O}_3$ , is also made using a sol gel method [*Visser*, 1999]. The melt is added to the polycrystalline samples by placing a thin layer of crushed glass powder onto the polycrystalline sample surface and heating over a period of several hours at the melting temperature of the glass ( $T_m = 1475^\circ\text{C}$ ). At this temperature, the melt becomes homogeneously distributed through the sample, and sintering reduces the remaining air filled porosity. During infiltration of the melt, the sample is maintained under vacuum, to reduce the amount of air-filled pores in the sample. In contrast, samples with melt fractions 0.01 and 0.015 are prepared by mixing the forsterite-enstatite powder produced in the sol gel process with the above glass powder. The forsterite-enstatite-glass mixture is subsequently cold pressed and sintered in the manner employed by *McDonnell et al.* [2002], first for 40 min at  $1400^\circ\text{C}$  to reduce the porosity, and then for a further few hours at  $1475^\circ\text{C}$  to melt the glass particles. This final sintering stage is again done with the sample under vacuum, though it is not possible to remove all the air, because some remains trapped in intragranular or nonconnected pores. After sintering and melt infiltration, both types of samples contain around 2% air-filled porosity in approximately circular pores. In a previous study, we showed that this porosity does not influence electrical conductivity measurements [*ten Grotenhuis et al.*, 2004]. Note however that the grain size does increase significantly during preparation of the samples from 1  $\mu\text{m}$  to 25–50  $\mu\text{m}$  (Table 1). To check the whether the microstructure of the samples is developed into a steady state melt texture after a few hours, we also heated two samples with 1.5 and 3.5% melt for 80 hours at  $1475^\circ\text{C}$  and studied them with SEM.

[9] From the phase diagram for the system studied [*Osborn and Muan*, 1960], slight changes in the melt composition and content are expected to occur during the preparation of the samples. However, the conductivity of the melt is insensitive to small changes in the melt composition, because the diffusion coefficients of the different elements in the melt, which determine the conductivity, are very uniform [*Kress and Ghiorso*, 1993]. The melt content

of the samples was checked after the experiments. In all our experiments, the amount of melt added to the samples is similar to the amount detected after the experiments with SEM (Table 1).

## 2.2. Impedance Measurements on Partially Molten Samples

[10] Electrical impedance measurements on the disc-shaped partially molten samples are made at a fixed temperature of  $1475^\circ\text{C}$ , the melting temperature of the added glass phase. Measurements are done in the frequency range  $10^0$ – $10^6$  Hz, taking 6 measurements per decade, using a Solatron 1260 impedance/gain phase analyzer with a model 1296 dielectric interface. The measured complex impedance

$$Z^* = Z' - jZ'' \quad (1)$$

can be represented in term of an ohmic resistance ( $Z'$ ) and capacitive reactance ( $Z''$ ), where  $Z'$  corresponds to the resistance ( $R$ ) and  $Z'' = 1/\omega C$ , with  $\omega$  as the angular frequency and  $C$  as capacitance.

[11] The impedance measurements are performed inside a vertically mounted, controlled atmosphere furnace, with air flushing through at one atmosphere total pressure [see also *ten Grotenhuis et al.*, 2004]. Platinum electrodes, made of 0.5 mm thick sheet, and guard ring, made of 0.5 mm thick platinum wire, are pressed onto the disc-shaped samples using alumina backing plates held in place by hollow, alumina push rods. The alumina tubes holding the electrode leads are shielded with Pt paint, connected to ground, to eliminate noise from the power supply. A two-electrode measurement method with guard ring is applied. The sample temperature is measured using two thermocouples located directly above and below the sample. Before making the conductivity measurements, the samples are dried at a temperature of  $800^\circ\text{C}$  over a period of 2 hours. Each sample is measured several times at 20 min intervals, while held at  $1475^\circ\text{C}$ , to ensure that the melt distribution is well equilibrated.

## 2.3. Impedance Measurements on the Pure Melt

[12] To obtain information on the melt properties, independently of the partially molten samples, the conductivity of the melt is measured between 1300 and  $1480^\circ\text{C}$  with a separate set up consisting of one cylindrical Pt electrode with an outer radius of 2.1 mm located centrally in a circular platinum cup with an inner radius of 6.8mm, serving as a

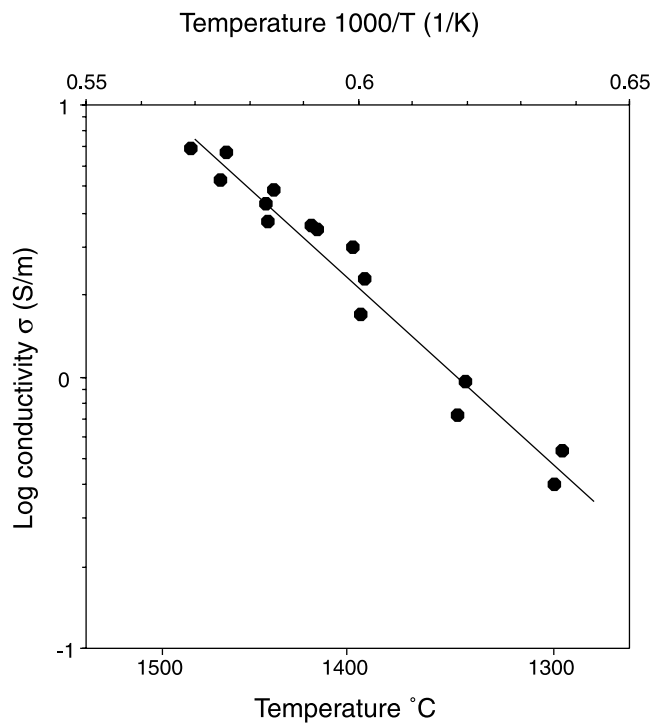


**Figure 1.** Temperature dependence of melt conductivity ( $\sigma_m$ ) measured between 1300 and 1480°C, with best fit.

second electrode. The distance from the base of the central electrode to the bottom of the cup is about twice the distance to the sides of the cup. This geometry minimizes interaction between the central electrode and the bottom of the cup. The measurements were again performed with a Solatron 1260 impedance analyzer.

#### 2.4. Microstructural Analysis

[13] The microstructure of the samples is analyzed after the conductivity measurements with a FEI Field emission XL30FEG SEM, using backscatter electron (BSE) and secondary electron (SE) imaging, as well as electron back scatter diffraction (EBSD). The difference in atomic number between the melt and the grains is insufficient to recognize the melt automatically on the BSE images. However, the EBSD images allow automatic analysis of the melt distribution and can reveal any relation between the crystallography of the grains and melt pore/layer geometry. The EBSD indexing and image analysis is done with HKL channel 5 software. For the samples selected for EBSD, an area of 200 by 250  $\mu\text{m}$  is analyzed, which represents approximately 40–50 grains. The step size for the EBSD maps is 0.5  $\mu\text{m}$ , which is a compromise between adequate resolution and the need to cover a large enough area in a reasonable time. The minimum thickness of melt layers that can be detected using this method is about 200 nm.

### 3. Results

#### 3.1. Impedance Data

[14] The conductivity of the melt as a function of temperature is shown in Figure 1. A linear dependence of conductivity on reciprocal temperature is observed for the melt, implying an Arrhenius relation. The melt conductivity

at 1475°C is estimated, from the regression line shown, to be  $7.53 \pm 0.38$  S/m. The impedance signature of the partially molten samples reaches a stable value after 20–40 min at 1475°C. The stable impedance data sets are plotted in the complex plane in Figure 2. The data show one arc at the highest frequencies. An additional depressed arc is observed in all samples at low frequencies, but is usually poorly developed and shows no dependence upon grain size, melt content or sample thickness. This low-frequency arc is accordingly interpreted as an effect of the electrodes, and the high-frequency arc as reflecting the sample properties. Conductivity values were computed from impedance values  $Z'$  taken at the frequency where the phase shift is closest to zero. The bulk conductivity of the partially molten samples is 1–2.5 orders of magnitude lower than the conductivity of the melt (Figure 3), and 1.5–3 orders of magnitude higher than predicted for a melt-free forsterite sample, with a grain size of 25  $\mu\text{m}$  at 1475°C, using the data and model presented by *ten Grotenhuis et al.* [2004]. As shown in Figure 3, there is an increase in bulk conductivity with increasing melt fraction from about 0.02 S/m, for the samples with melt fraction 0.01, to 0.71 S/m, for the sample with melt fraction 0.1.

#### 3.2. Microstructural Observations

[15] The microstructure of the quenched samples is shown in Figure 4 (BSE images), and Figure 5 (EBSD maps). First of all, the melt content in the samples was estimated with the SEM images and EBSD maps. The detected amount of melt was very close to the amount added to the samples (Table 1). Subsequently, the grain size distribution of the samples was determined, using the EBSD maps. According to *Faul* [1997], a narrow grain size distribution with the peak close to the mean grain size is caused by grain growth. Because grain growth and grain-scale melt distribution are both driven by interface energy

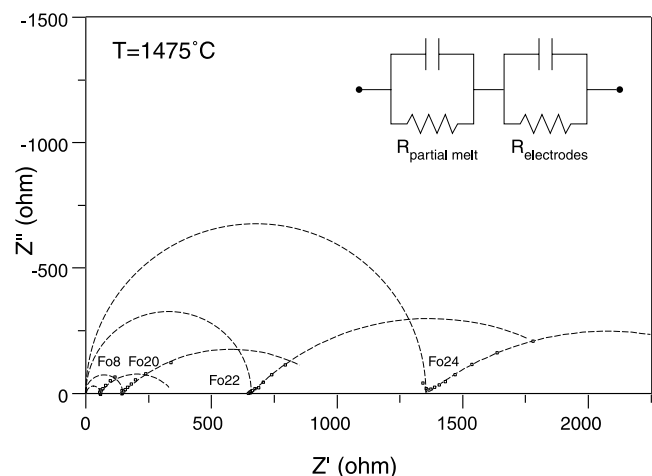


**Figure 2.** Impedance data in complex plane for samples Fo8, Fo20, Fo22, and Fo24 with melt fractions 0.05, 0.035, 0.015, and 0.01, respectively, taken after 40 min at 1475°C. The dashed curves through the data are theoretical curves obtained with the equivalent circuit shown at the top right. The measurements show one clear impedance arc at the highest frequencies, which is caused by the interconnected melt path.

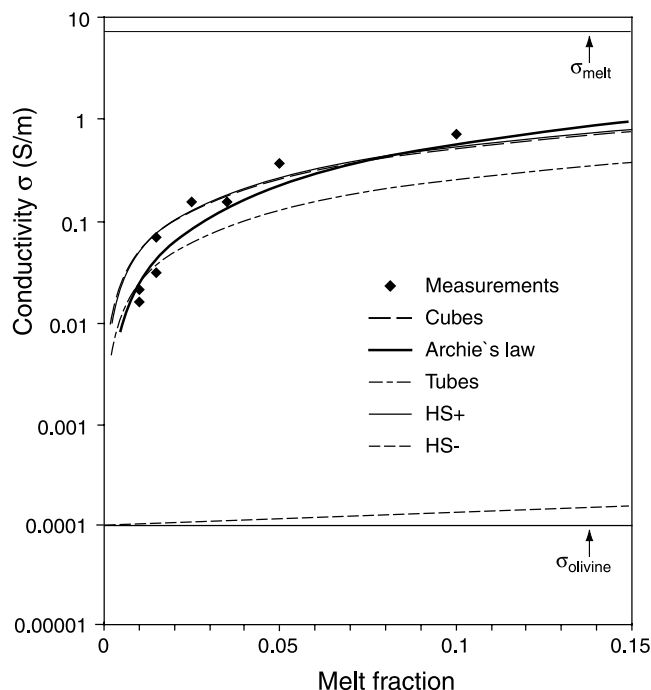


**Figure 3.** Experimental data on bulk electrical conductivity of the partially molten samples plotted as a function of the melt fraction (diamonds). Curves represent conductivity predicted by inserting the measured melt conductivity into the melt distribution models shown. Input data for the melt conductivity and conductivity of the olivine (0.0001 S/m) are also presented.

reduction, a narrow grain size distribution with the peak close to the mean grain size is an indicator for a steady state melt distribution. In Figures 5c and 5d the histograms of the grain size distributions of samples Fo24 and Fo9 are shown, with the grain size normalized by the mean grain size. Both samples show a narrow grain size distribution with the peak close to the mean grain size, indicating a steady state melt distribution. To check whether the samples had reached a steady state melt distribution during the conductivity measurements, two samples were heated 80 hours at 1475°C. SEM back scatter images of these samples are shown in Figure 6. The microstructures of the samples are very similar to the microstructures of the samples with the same amount of melt heated for only 2–4 hours.

[16] In every section examined, all of the triple junctions between three forsterite grains contain melt. This observation is consistent with previous studies on melt distribution in mantle rocks [Toramaru and Fujii, 1986; Hirth and Kohlstedt, 1995; Cmiral et al., 1998; Walte et al., 2003]. In addition, several trends are visible in the melt distribution, with increasing melt content. For example, the number of large multigrain-bounded melt pools and melt layers between grains increases significantly (Figure 4). Also, while the effect of anisotropy is apparent in all samples, it is most noticeable in the samples with higher melt fraction, through the formation of flat, crystallographically controlled, grain-melt interfaces (Figure 4). To quantify the fraction  $\varphi$  of grain interface wetted by melt, the total length of detectable grain-melt interface is divided by the total grain-grain plus grain-melt interface length. We did not

separate melt in triple junctions from melt in two-grain boundaries in this approach, because the transition from triple junction to grain boundary is usually gradual, especially at higher melt fractions. The fraction  $\varphi$  is calculated by placing a square grid with 1  $\mu\text{m}$  spacing over the EBSD images. At each interface, we record whether it is a grain-grain interface or a grain-melt interface. The thus estimated fraction  $\varphi$  of melt-wetted grain interface increases significantly with increasing melt fraction from 0.32 at melt fraction 0.01 to 0.90 at melt fraction 0.1 (Figure 7a). To compare our data with the melt distribution in deformed partially molten samples of Hirth and Kohlstedt [1995] we also counted the number fraction of grain boundaries completely wetted by melt. The microstructural data reported by Hirth and Kohlstedt [1995] and our data are in good agreement (Figure 7a). The number of grain boundaries completely wetted by melt is obviously lower than the fraction  $\varphi$ . At melt fraction 0.01, 3% of the grain boundaries are completely wetted, increasing to 42% at melt fraction 0.1. Interestingly, the minor amount of enstatite in the samples has very little effect on the melt distribution. Enstatite-forsterite grain boundaries are in general melt free, and Fo-Fo-En triple junctions are either melt free or contain a small amount of melt [cf. Toramaru and Fujii, 1986]. Moreover, most enstatite is disappeared because of chemical re-equilibration in the samples with 5 and 10% melt. This basically means that the minor amount of enstatite in our samples can be ignored in considering the melt distribution. As already indicated, flat crystal faces are most frequently observed in the samples with the highest melt fractions. Contrary to expectations, however, they are not preferentially associated with melt layers or pools. Some flat crystal faces form part of a dry grain-grain interface (Figure 5).

## 4. Discussion

[17] Electrical conductivity data for partially molten samples with melt fractions between 0.01 and 0.1 show an increase of conductivity with increasing melt content. We will now compare our results with the predictions of models based on different geometrical melt distributions, considering both conductivity and microstructural aspects in making this comparison. We also compare our results with porosity-permeability models constructed for partially molten rocks.

### 4.1. Comparison With Geometrical Models of Electrical Conductivity

[18] Numerous geometrical models based on simplified melt distributions have been developed to calculate the effective conductivity ( $\sigma_t$ ) of a partially molten sample as a function of the melt fraction ( $X_m$ ), conductivity of the solid phase ( $\sigma_s$ ) and conductivity of the melt phase ( $\sigma_m$ ). Our data are compared with some of these models in order to get an idea of the melt distribution around the grains while the samples are at high temperature. The models considered correspond to different melt distributions in the samples, with either melt along the triple junctions, melt along the grain boundaries or melt in isolated pocket. The data are compared to four different models:

#### 4.1.1. Cubes Model [Waff, 1974]

[19] In this model cubic grains with a low conductivity are all the same size and are surrounded by a high-

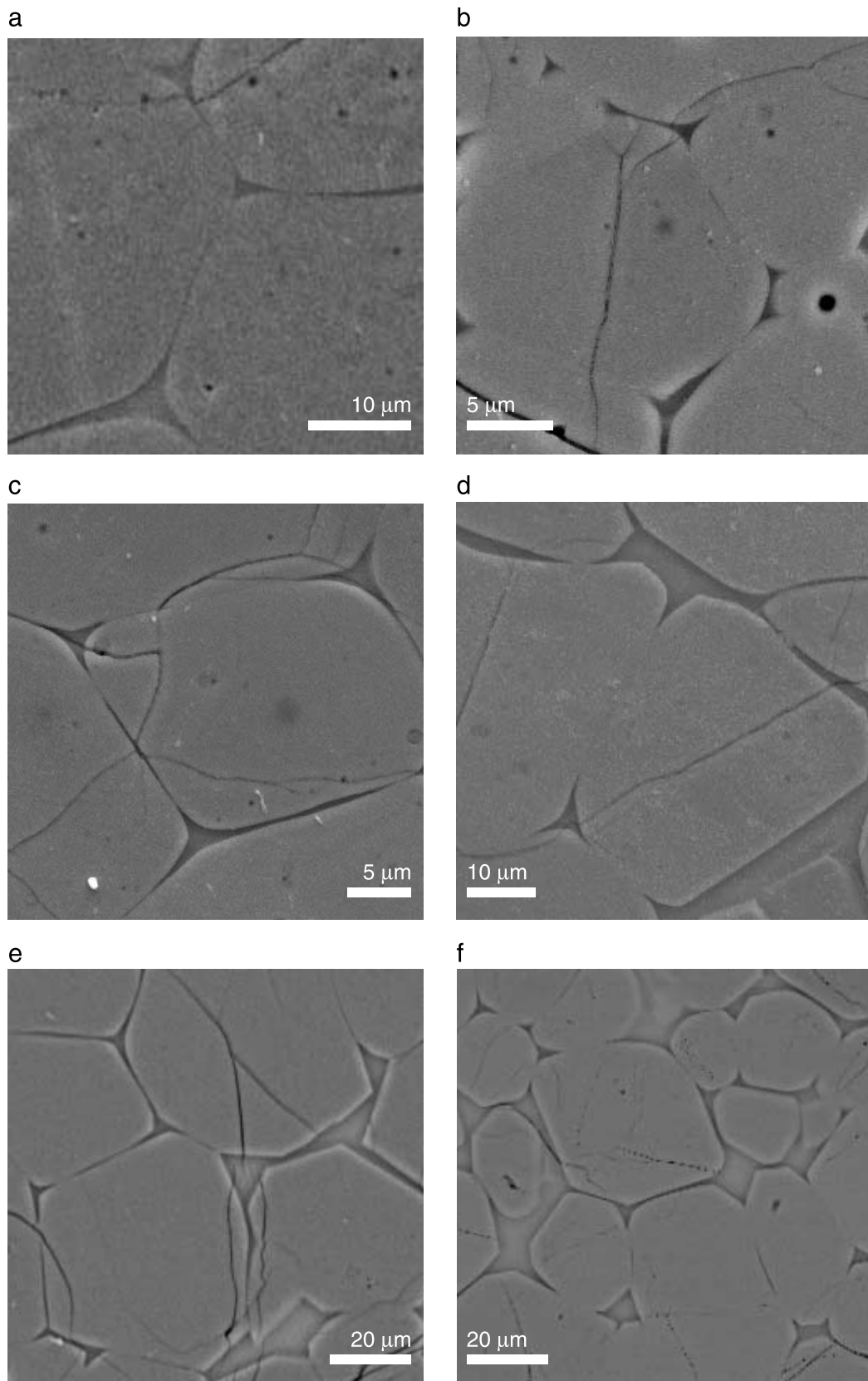


**Figure 4.** SEM backscatter images of samples (a) Fo24, melt fraction 0.01; (b) Fo23, melt fraction 0.015; (c and d) Fo20, melt fraction 0.035; (e) Fo8, melt fraction 0.05; and (f) Fo9, melt fraction 0.1. Black lines on the images are cracks developed during quenching after the conductivity measurements. Notice the increase in number of wetted two-grain boundaries with increasing melt content. Distinct crystal facets can be observed in all samples.

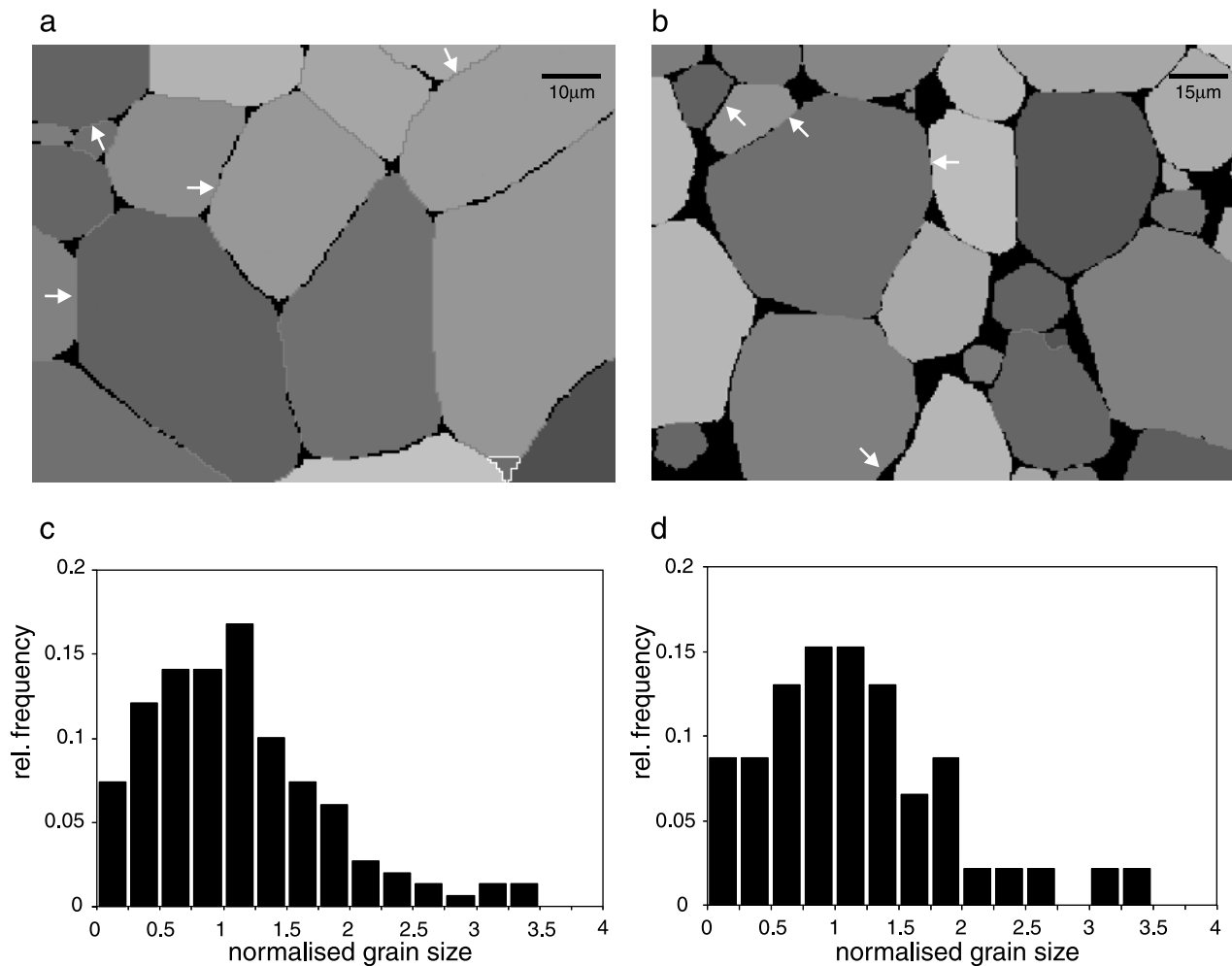


**Figure 5.** EBSD images of samples (a) Fo24 and (b) Fo9, with melt fractions 0.01 and 0.1, respectively. Different gray levels represent different crystallographic orientations. In black are the “zero solutions” in the EBSD analysis, which represent the melt. The flat interfaces indicated by white arrows are crystallographic controlled. The small white-rimmed grain at the bottom of Figure 5a is an enstatite grain. Also shown are grain size distributions normalized by the mean grain size of samples (c) Fo24 and (d) Fo9, showing a narrow grain size distribution with the peak close to the mean grain size.

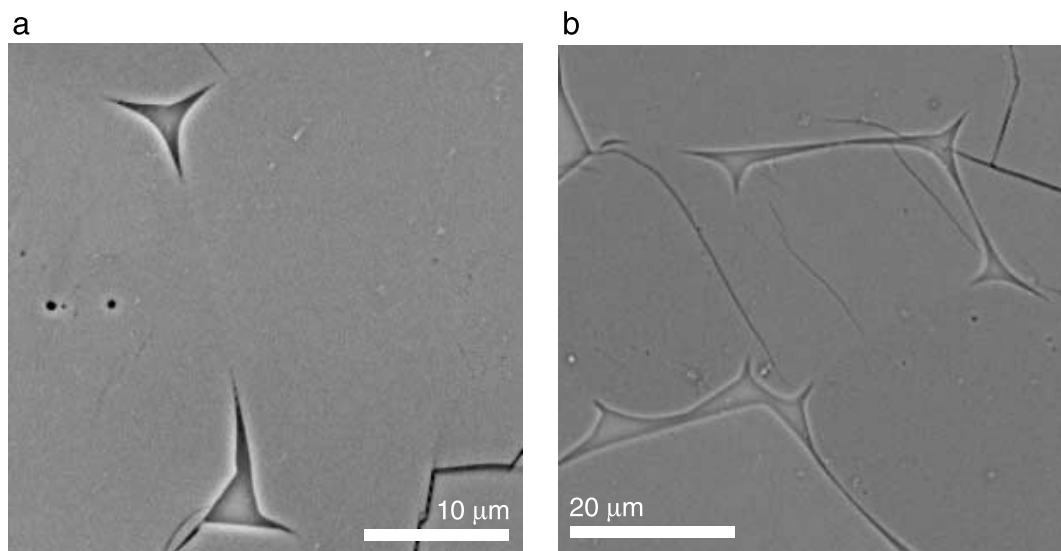


**Figure 6.** SEM backscatter images showing melt distribution in samples (a) Fo28 and (b) Fo27, with melt fractions 0.015 and 0.035, respectively.

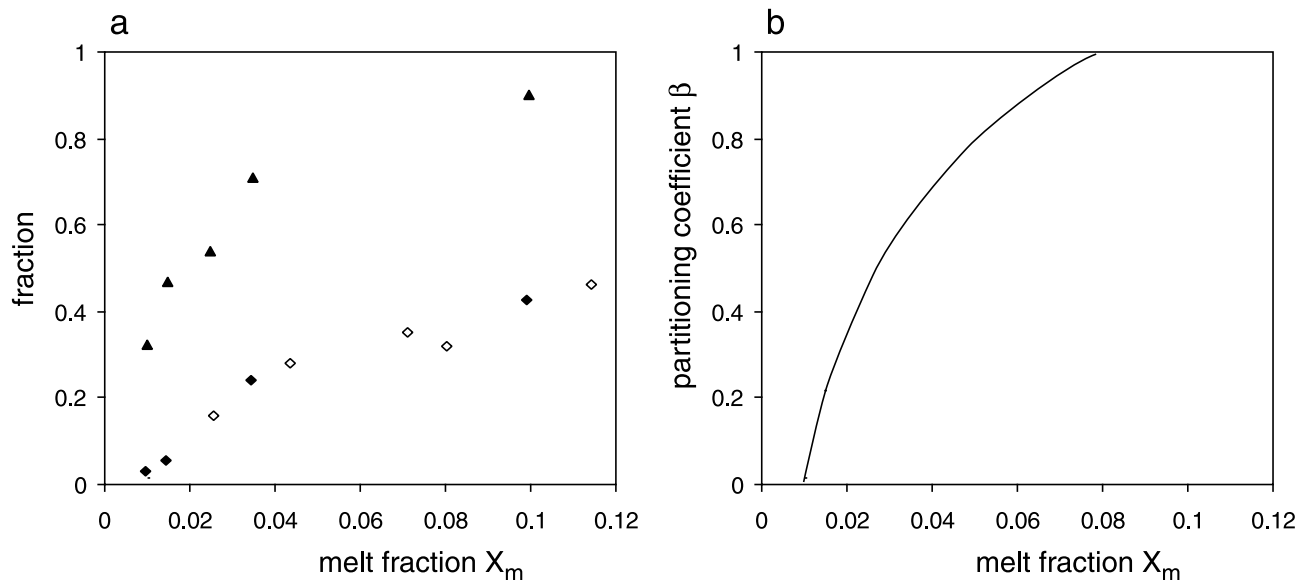


**Figure 7.** (a) Fraction of melt-filled grain boundary length ( $\varphi$ , triangles), fraction of completely wetted grain boundaries (solid diamonds), and fraction of completely wetted grain boundaries in samples of Hirth and Kohlstedt [1995] (open diamonds). (b) Partitioning of the melt between tubes ( $\beta = 0$ ) and layers ( $\beta = 1$ ) implied by fitting Archie's law to our data with  $C = 1.64$  and  $n = 1.34$ .

conductivity melt layer of uniform thickness (Figure 8). This geometrical model is representative for melt distributed in layers along the grain boundary. The effective conductivity according to this model is

$$\sigma_t = \left[ 1 - (1 - X_m)^{\frac{2}{3}} \right] \sigma_m \quad (2)$$

#### 4.1.2. Spheres Model

[20] In this model (usually called Hashin-Shtrikman upper bound or Maxwell model, [Waff, 1974], the matrix consists of a high-conductivity melt phase surrounding spherical inclusions with a lower conductivity, which represent the less conductive grains (Figure 8). The spherical grains are isolated from each other by the melt, so this model is representative for melt distributed along grain boundary and filling triple junctions. The effective conductivity is given by

$$\sigma_t = \sigma_m + \frac{(1 - X_m)}{1/(\sigma_s - \sigma_m) + X_m/3\sigma_m} \quad (3)$$

The Hashin Shtrikman lower bound, the opposite case of the HS upper bound, represents isolated spheres of high-conductivity melt in a low-conductivity matrix representing the grains, and takes the form

$$\sigma_t = \sigma_s + \frac{X_m}{1/(\sigma_m - \sigma_s) + (1 - X_m)/3\sigma_s} \quad (4)$$

#### 4.1.3. Tubes Model [Grant and West, 1965; Schmeling, 1986]

[21] In this model the melt is distributed in equally spaced tubes within a rectangular network (Figure 8). This model represents the case that melt is distributed in a network

along the triple junctions, but with unwetted two-grain junctions, and is written

$$\sigma_t = \frac{1}{3}X_m\sigma_m + (1 - X_m)\sigma_s \quad (5)$$

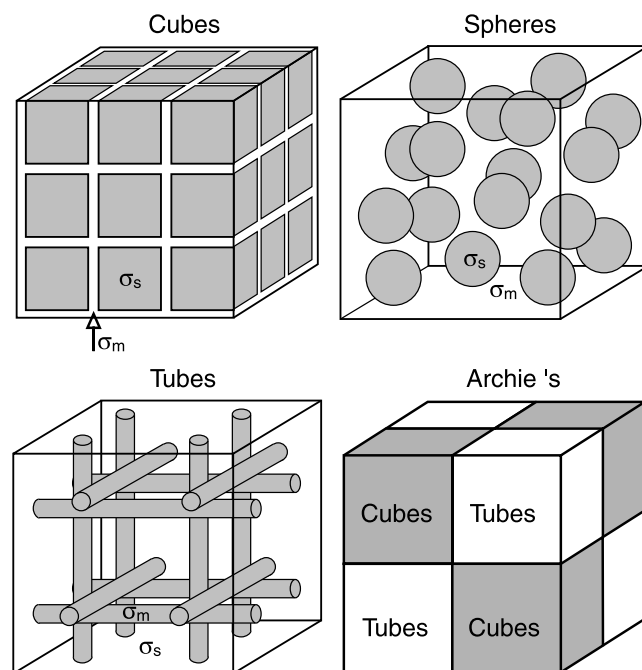


**Figure 8.** Sketches of the melt distribution according to different geometric models. Archie's law can be interpreted as describing a mix between two different models, in this study as a mixture between the "cubes" and the "tubes" models.



**Table 2.** Correlation Coefficients ( $R^2$ ) for the Different Geometrical Models to  $\log(\sigma_t)$ 

Geometrical Model	$R^2$
Archie's law with $C = 1.47$ and $n = 1.30$	0.98
Cubic	0.95
Spheres or HS+	0.95
Tubes	0.96

#### 4.1.4. Archie's Law [Watanabe and Kurita, 1993]

[22] This law is not a geometrical model, but an empirical relation between melt conductivity and bulk conductivity. It is based on a resistor network theory and allows for a change in connectivity with increasing melt fraction. This relation is commonly applied to represent connectivity in sandstones saturated with water, and is given by

$$\sigma_t = CX_m^n \sigma_m \quad (6)$$

The properties of the melt in these models are assumed everywhere the same, and the melt is assumed to be homogeneously distributed through the sample. In all models, the effective conductivity is described as a function of the melt conductivity and the melt fraction. The grain size is not important in these theoretical models, because the properties of the melt are assumed to be independent of the thickness of the melt layers or films between the grains. The conductivity of the solid plays only a minor role in these models, because the conductivity of the melt is at least 3 orders of magnitude higher. Only at very small melt fractions ( $<0.001$ ) does the conductivity of the solid grains start to play a role. Input data for the models are the conductivity of the melt, presented above, and the conductivity of the solid, based on the results from *ten Grotenhuis et al.* [2004]. The resulting bulk conductivity as a function of the melt fraction is plotted in Figure 3 alongside our results for the different samples.

[23] From Figure 3 it is evident that the bulk conductivities predicted by the Spheres and Cubes models are very similar. The Tubes model predicts a lower conductivity at equal melt fraction. The bulk conductivity of the samples with different melt fractions is best represented by the Spheres or Cubes model for melt fractions  $\geq 0.025$ , and by the Tubes model for samples with melt fraction  $< 0.015$ . *Roberts and Tyburczy* [1999] found the Hashin-Shtrikman upper bound to be the best model for their olivine samples with 5% MORB, which agrees very well with our conclusions for samples with melt fractions above 0.025. The conclusion that the tubes model fits best with the samples with lower melt contents on the other hand agrees well with the melt distribution predicted by *Wark and Watson* [1998]. Archie's law best represents the total data set; that is, it has the highest correlation coefficient,  $R^2$  (Table 2), because it represents a mixture of different models. For the complete data set, the best fit parameters for Archie's law are  $C = 1.47$  and  $n = 1.30$ . By comparison, the constants found by *Watanabe and Kurita* for the system ice and liquid KCl are  $C = 0.02-0.30$  and  $n = 1.34-1.74$ , for a range of KCl concentrations between 0.2 and 0.8 wt%, and melt fractions less than 0.2. *Watanabe and Kurita* [1993] concluded that for their system Archie's law indicates a change from a relatively large portion of isolated pockets, at low melt

fraction, to more melt in triple junction tubes, at high melt fraction. For our system, the  $n$  value is very similar and the  $C$  value is higher, suggesting a similar change in melt distribution with melt content, but with generally better interconnection of the melt. To describe the melt distribution in our samples, Archie's law can be used by viewing it as a mixture between the Tubes and Cubes or Spheres model for melt fractions between 0.01 and 0.1, because most of the data are very close to these models. We have calculated the partitioning of conductivity between tubes and layers in the cubes model using the geometric mean formula

$$\sigma_{total} = \sigma_m * 1.47X_m^{1.30} = \sigma_{tubes}^{(1-\beta)} * \sigma_{cubes}^{\beta} \quad (7)$$

where the factor  $\beta$  determines the partitioning in tubes and layers. For  $\beta = 0$  all the melt lies in triple junction tubes, and for  $\beta = 1$  one all the melt is in grain boundary layers. The partitioning between tubes and layers as a function of the melt fraction, based on Archie's law with  $C = 1.47$  and  $n = 1.30$  is given in Figure 7b. Below a melt fraction of 0.01, all melt is predicted to be in the triple junction network. Between melt fractions 0.01 and 0.08, there is a gradual increase in the importance of grain boundary melt layers, and above 0.08 all melt is predicted to be in grain boundary melt layers.

#### 4.2. Microstructural Data

[24] The microstructural observations of our samples with SEM and EBSD lead to similar conclusions. The fraction  $\varphi$  of grain interface wetted by melt and the fraction of two-grain boundaries completely filled with melt both increase significantly with increasing melt content in our samples. The fraction of two-grain boundaries completely filled with melt is less useful to describe the microstructure for conductivity experiments than the fraction  $\varphi$ , because there is no differentiation between partly dry grain boundaries, which can contribute significantly to the total conductivity, and completely melt free grain boundaries, which are not contributing to the total conductivity. However, at high melt fractions still numerous two-grain boundaries are not completely wetted. The presence of partly dry grain boundaries at higher melt contents does not seem to have an effect on the conductivity. One of the reasons for this is the presence of grain boundaries that are completely free of melt (Figures 4d, 4e, and 5b), where the two neighboring grains are effectively one grain as seen by the conductivity measurements. Other melt microstructures, like melt pools and dry Fo-Fo-En triple junctions, apparently also play a minor role in determining the electrical conductivity of the samples. We cannot exclude the presence of nanometer-scale melt films on grain boundaries, because the resolution in SEM images and EBSD analysis is insufficient for detection of these films. However, the resemblance between conclusions drawn from the conductivity experiments and from microstructural observations suggests that such films are most likely absent in our samples, or do not influence the conductivity measurements.

#### 4.3. Comparison With Porosity-Permeability Models

[25] *Faul* [1997, 2001] proposed a porosity-permeability model that predicts permeability of partially molten mantle

rocks. This model is based on a separation of the melt into disc-shaped pools containing most of the melt and into a network along the triple junctions containing about 10% of the melt. The model of *Faul* [1997] leads to a sharp increase in permeability of about 4 orders of magnitude at around 2% melt, because at this point the discs become interconnected. On the basis of this model, the increase in electrical conductivity should be 1.5 orders of magnitude at around 2% melt. *Wark and Watson* [1998] proposed a porosity-permeability model based on measurements of quartz-fluid aggregates, which predicts a gradual increase of permeability with increasing porosity. Numerical simulations by *von Bargaen and Waff* [1986] have predicted a similar continuous porosity-permeability relation. Neither of these studies take the disequilibrium melt structures frequently observed in olivine into account.

[26] Our conductivity results could be interpreted in terms of a discontinuous porosity-permeability functions with a change from melt tubes to melt layers at  $X_m = 0.015-0.02$  (Figure 3). Our microstructures show however that there is a gradual increase in the melt present in layers and intersperses. A continuous porosity-permeability relation is also consistent with our data. However, our data suggest a faster increase in permeability between melt fractions 0.01 and 0.1 than implied by the continuous porosity-permeability functions of *Wark and Watson* [1998] and *von Bargaen and Waff* [1986], because in our samples the fraction  $\varphi$  of grain interface wetted by melt, and the fraction of two-grain boundaries completely filled with melt, both increase significantly with increasing melt fraction. According to *Hirth and Kohlstedt* [1995] the anisotropy in solid-liquid interface energy alone is enough to cause complete wetting of two-grain boundaries in olivine-melt systems. The higher fraction  $\varphi$  of wetted grain interface and wetted two-grain boundaries at higher melt fractions can be explained by the lower chemical potential of the melt-grain interface due to the lower mean curvature of this interface at higher melt fractions. The lower chemical potential favors the formation and lifetime of metastable features like melt layers. Therefore a regular network of triple junction tubes exists at low melt fractions. At higher melt fractions melt-filled grain boundaries and melt lenses are more frequent and these structures will start dominating rock properties that are determined by the grain-scale melt distribution.

#### 4.4. Application for the Interpretation of Electromagnetic Measurements

[27] Our version of Archie's law describing the relation between melt distribution and melt fraction can be used to deduce the melt fraction and the melt distribution in melt-bearing regions in the mantle from electromagnetic measurements. We will illustrate this briefly with reference to a study from the Juan de Fuca midocean ridge by *Jegen and Edwards* [1998]. The minimum conductivity estimated for a conventional mantle upwelling zone beneath the Juan de Fuca ridge is 0.2 S/m. Using the expressions for the Hashin-Shtrikman upper bound and Archie's law from *Schmeling* [1986] and a melt conductivity of 10 S/m, *Jegen and Edwards* [1998] estimated minimum melt fractions of 0.03 (HS+) and 0.14 (Archie's law). Using our version of Archie's law, we find that a minimum melt fraction of 0.037 can explain conductivities of 0.2 S/m.

With this melt fraction, about 70% of the melt would be present in two-grain boundary layers (see Figures 4c, 4d, and 7a).

## 5. Conclusions

[28] In this study the changes in melt distribution with increasing melt fraction in synthetic, partially molten, iron-free olivine rocks, with melt fraction between 0.01 and 0.1, are determined with electrical conductivity measurements and microstructural investigation, involving scanning electron microscopy (SEM) and electron backscatter diffraction (EBSD). The electrical conductivity data are compared with the predictions of geometric models for melt distribution. The electrical conductivity of the partially molten samples is best described by Archie's law ( $\sigma_{\text{sample}}/\sigma_{\text{melt}} = CX_m^n$ ) with parameters  $C = 1.47$  and  $n = 1.30$ , which in this case describes a gradual change in the melt distribution from network of triple junction tubes with almost all grain boundaries free from melt layers, at a melt fraction of 0.01, to a network of grain boundary melt layers, at a melt fraction of 0.1. The microstructural data confirm this conclusion, because the fraction of grain interface wetted by melt increases significantly between melt fractions 0.01 and 0.1.

[29] **Acknowledgments.** G. M. Pennock is thanked for her assistance with the EBSD analyses. G. Kastelein and P. van Krieken are thanked for their assistance with the sample preparation and conductivity experiments. The Netherlands Research Centre for Integrated Solid Earth Sciences (ISES) financially supported this work.

## References

- Bulau, J. R., and H. S. Waff (1979), Mechanical and thermodynamic constraints on fluid distribution in partial melts, *J. Geophys. Res.*, *84*(B11), 6102–6108.
- Cmiral, M., J. D. Fitz Gerald, U. H. Faul, and D. H. Green (1998), A close look at dihedral angles and melt geometry in olivine-basalt aggregates: A TEM study, *Contrib. Mineral. Petrol.*, *130*, 336–345.
- de Kloe, P. A. (2001), Deformation mechanisms and melt nano-structures in experimentally deformed olivine-orthopyroxene rocks with low melt fractions, *Geol. Ultraaetina 201*, Univ. Utrecht, Utrecht, Netherlands.
- de Kloe, R., M. R. Drury, and H. L. M. van Roermund (2000), Evidence for stable grain boundary melt films in experimentally deformed olivine-orthopyroxene rocks, *Phys. Chem. Miner.*, *27*, 480–494.
- Drury, M. R., and J. D. Fitz Gerald (1996), Grain boundary melt films in an experimentally deformed olivine-orthopyroxene rock: Implications for melt distribution in upper mantle rocks, *Geophys. Res. Lett.*, *23*(7), 701–704.
- Faul, U. H. (1997), Permeability of partially molten upper mantle rocks from experiments and percolation theory, *J. Geophys. Res.*, *102*(B5), 10,299–10,311.
- Faul, U. H. (2000), Constraints on the melt distribution in anisotropic polycrystalline aggregates undergoing grain growth, in *Physics and Chemistry of Partially Molten Rocks*, edited by N. Bagdassarov, D. Laporte, and A. B. Thompson, pp. 67–92, Springer, New York.
- Faul, U. H. (2001), Melt retention and segregation beneath mid-ocean ridges, *Nature*, *410*, 920–923.
- Faul, U. H., D. R. Toomey, and H. S. Waff (1994), Intergranular basaltic melt is distributed in thin, elongated inclusions, *Geophys. Res. Lett.*, *21*(1), 29–32.
- Grant, F. S., and G. F. West (1965), Introduction to the electrical methods, in *Interpretation Theory in Applied Geophysics*, edited by R. R. Shrock, pp. 385–401, McGraw-Hill, New York.
- Hashin, Z., and S. Shtrikman (1962), A variational approach to the theory of the effective magnetic permeability of multiphase materials, *J. Appl. Phys.*, *33*, 3125–3131.
- Hiraga, T., I. M. Anderson, M. E. Zimmerman, S. Mei, and D. L. Kohlstedt (2002), Structure and chemistry of grain boundaries in deformed, olivine + basalt and partially molten lherzolite aggregates: Evidence of melt-free grain boundaries, *Contrib. Mineral. Petrol.*, *144*, 163–175.

- Hirth, G., and D. L. Kohlstedt (1995), Experimental constraints on the dynamics of the partially molten upper mantle: Deformation in the diffusion creep regime, *J. Geophys. Res.*, *100*(B2), 1981–2001.
- Jegen, M., and R. N. Edwards (1998), The electrical properties of a 2D conductive zone under the Juan de Fuca ridge, *Geophys. Res. Lett.*, *25*(19), 3647–3650.
- Kingery, W. D., H. K. Bowen, and D. R. Uhlmann (1976), *Introduction to Ceramics*, 1032 pp., John Wiley, Hoboken, N. J.
- Kress, V. C., and M. S. Ghiorso (1993), Multicomponent diffusion in MgO-Al<sub>2</sub>O<sub>3</sub>-SiO<sub>2</sub> and CaO-MgO-Al<sub>2</sub>O<sub>3</sub>-SiO<sub>2</sub> melts, *Geochim. Cosmochim. Acta*, *57*, 4453–4466.
- Laporte, D., and A. Provost (2000), Equilibrium geometry of a fluid phase in a polycrystalline aggregate with anisotropic surface energies: Dry grain boundaries, *J. Geophys. Res.*, *105*(B11), 25,937–25,953.
- McDonnell, R. D., C. J. Spiers, and C. J. Peach (2002), Fabrication of dense forsterite-enstatite polycrystals for experimental studies, *Phys. Chem. Miner.*, *29*, 19–31.
- McKenzie, D. (1984), The generation and compaction of partially molten rock, *J. Petrol.*, *25*, 713–765.
- Osborn, E. F., and A. Muan (1960), *Phase Equilibrium Diagrams of Oxide Systems*, Am. Ceram. Soc., Columbus, Ohio.
- Roberts, J. J., and J. A. Tyburczy (1999), Partial-melt electrical conductivity: Influence of melt composition, *J. Geophys. Res.*, *104*(B4), 7055–7065.
- Sato, H., and Y. Ida (1984), Low frequency electrical impedance of partially molten gabbro: The effect of melt geometry on electrical properties, *Tectonophysics*, *107*, 105–134.
- Schmeling, H. (1986), Numerical models on the influence of partial melt on elastic, anelastic and electric properties of rocks. part II: Electrical conductivity, *Phys. Earth Planet. Inter.*, *43*, 123–136.
- ten Grotenhuis, S. M., M. R. Drury, C. J. Peach, and C. J. Spiers (2004), Electrical properties of fine-grained olivine: Evidence for grain boundary transport, *J. Geophys. Res.*, *109*, B06203, doi:10.1029/2003JB002799.
- Toramaru, A., and N. Fujii (1986), Connectivity of melt phase in a partially molten peridotite, *J. Geophys. Res.*, *91*(B9), 9239–9252.
- Turcotte, D. L., and J. P. Morgan (1992), The physics of magma migration and mantle flow beneath a mid-ocean ridge, in *Mantle Flow and Melt Generation at Mid-Ocean Ridges*, *Geophys. Monogr. Ser.*, vol. 71, edited by J. Phipps Morgan, D. K. Blackman, and J. M. Sinton, pp. 155–182, Washington, D. C.
- Visser, H. J. M. (1999), Mass transfer processes in crystalline aggregates containing a fluid phase, *Geol. Ultraelectra 174*, Univ. Utrecht, Utrecht, Netherlands.
- von Bargen, N., and H. S. Waff (1986), Permeabilities, interfacial areas and curvatures of partially molten systems: Results of numerical computations of equilibrium microstructures, *J. Geophys. Res.*, *91*(B9), 9261–9276.
- Waff, H. S. (1974), Theoretical considerations of electrical conductivity in a partially molten mantle and implications for geothermometry, *J. Geophys. Res.*, *79*(26), 4003–4010.
- Waff, H. S., and J. R. Bulau (1979), Equilibrium fluid distribution in an ultramafic partial melt under hydrostatic stress conditions, *J. Geophys. Res.*, *84*(B11), 6109–6114.
- Waff, H. S., and U. H. Faul (1992), Effects of crystalline anisotropy on fluid distribution in ultramafic partial melts, *J. Geophys. Res.*, *97*(B6), 9003–9014.
- Walte, N. P., P. D. Bons, C. W. Passchier, and D. Koehn (2003), Disequilibrium melt distribution during static recrystallisation, *Geology*, *31*, 1009–1012.
- Wark, D. A., and E. B. Watson (1998), Grain-scale permeabilities of texturally equilibrated, monomineralic rocks, *Earth Planet. Sci. Lett.*, *164*, 591–605.
- Wark, D. A., C. A. Williams, E. B. Watson, and J. D. Price (2003), Reassessment of pore shapes in microstructurally equilibrated rocks, with implications for permeability of the upper mantle, *J. Geophys. Res.*, *108*(B1), 2050, doi:10.1029/2001JB001575.
- Watanabe, T., and K. Kurita (1993), The relationship between electrical conductivity and melt fraction in a partially molten system: Archie's law behaviour, *Phys. Earth Planet. Inter.*, *78*, 9–17.

---

M. R. Drury, C. J. Peach, C. J. Spiers, and S. M. ten Grotenhuis, Department of Earth Sciences, Utrecht University, PO Box 80021, NL-3508 TA Utrecht, Netherlands. (saskiatg@geo.uu.nl)